

# **Raman mapping and numerical simulation of calcium carbonates distribution in experimentally carbonated Portland cement cores**

Running title: Raman mapping and modelling of CaCO<sub>3</sub> distribution in cement

Plan:

1- Introduction

2- Materials and methods

2-1- Carbonation procedure

2-2- Characterization techniques

2-3- Numerical modelling

3- Phase characterization results

3-1- Main carbonation features

3-2- CaCO<sub>3</sub> polymorph distribution along the main diffusion path

4- Numerical simulations and Discussion

5- Concluding remarks

6- References

Corresponding author: Jérôme Corvisier

Mailing address: Laboratoire de Géologie, Ecole normale supérieure, CNRS-UMR8538

24, rue Lhomond 75231 – Paris Cedex 05 – France

Email address: [corvisier@geologie.ens.fr](mailto:corvisier@geologie.ens.fr)

Phone number: +33 1 44 32 22 90

Fax number: +33 1 44 32 22 00

Operating system: windows XP

Word-processor: Microsoft Word 2003

Number of characters: 42809

**Raman mapping and numerical simulation of calcium  
carbonates distribution in experimentally carbonated  
Portland cement cores**

Jérôme Corvisier<sup>1</sup>, Fabrice Brunet<sup>1</sup>, Antonin Fabbri<sup>1,2</sup>, Sylvain Bernard<sup>1</sup>, Nathaniel Findling<sup>1</sup>, Gaëtan  
Rimmelé<sup>3</sup>, Véronique Barlet-Gouédard<sup>3</sup>, Olivier Beyssac<sup>1</sup> & Bruno Goffé<sup>1,4</sup>

<sup>1</sup> Laboratoire de Géologie, Ecole normale supérieure, CNRS-UMR8538 - 24, rue Lhomond 75231 -  
Paris Cedex 05, France

<sup>2</sup> BRGM, GEO/G2R - 3, avenue Claude Guillemin 45060 - Orléans Cedex 2, France

<sup>3</sup> Schlumberger, SRPC - 1, rue Becquerel BP 202 F-92142 - Clamart, France

<sup>4</sup> CEREGE, CNRS-UMR6635 - Europôle de l'Arbois 13545 - Aix en Provence, France

Corresponding author: corvisier@yahoo.fr

## Abstract

The spatial distribution of  $\text{CaCO}_3$  polymorphs formed during the experimental carbonation of water saturated Portland cement cores (30-mm in diameter), with supercritical  $\text{CO}_2$  at  $90^\circ\text{C}$  and 30 MPa, has been investigated using Raman micro-spectrometry on polished sample sections and X-ray micro-diffraction. The three calcium carbonate polymorphs (calcite, aragonite and vaterite) were clearly distinguished using both techniques and their distribution along the main  $\text{CO}_2$  diffusion direction could be mapped at the millimetre scale using a dynamic line-scanning Raman mapping tool. The calcium carbonate 2-D distribution clearly shows that vaterite, the least stable of the three  $\text{CaCO}_3$  polymorphs, is mostly located in a 500- $\mu\text{m}$  wide ring ahead of the carbonation zone. This feature indicates that vaterite is the first  $\text{CaCO}_3$  polymorph to crystallize within the cement sample in the course of the carbonation process. The presence of a vaterite front indicates that local mineral-solution equilibration can be slower than species transport, even above ambient conditions, and that kinetics cannot be ignored in the cement carbonation process. By using calcite and vaterite precipitation kinetic data from the literature and assuming a water-mineral kinetics based on the Transition State Theory, the width of the vaterite front inferred from Raman mapping is reproduced with a purely diffusive 1D transport code when the vaterite dissolution coefficient is set to ca.  $1.6 \text{ mol.m}^{-2}.\text{h}^{-1}$ .

## 1. Introduction

The efficiency of underground  $\text{CO}_2$  storage either in deep saline aquifers or in depleted oil and gas fields mostly relies on the well-bore integrity. There are more and more lines of evidence, that Portland cement which is used as sealing material around the well-bore will react when exposed to  $\text{CO}_2$ -rich fluids under down-hole conditions. Both experimental simulations (Bruckdorfer, 1986; Barlet-Gouédard et al., 2006; 2007; in press; Duguid et al., 2006; Kutchko et al., 2007; Jacquemet et al., 2008; Rimmelé et al., 2008) and natural case (SACROC, Carey et al., 2007) show that Portland hydraulic cement pastes develop reaction fronts (carbonation and/or alteration) in  $\text{CO}_2$ -rich fluid environments which may affect their hydromechanical properties (Fabbri et al., 2009;). These fronts reflect a carbonation process which is mostly transport-limited owing to the high reactivity of Ca-bearing cement phases such as portlandite or calcium silicate hydrates (C-S-H) with

CO<sub>2</sub>-rich fluids. Potentially, this high-reactivity is convenient for numerical simulation since local equilibrium can then be considered (Moranville et al., 2004; Huet et al., 2008). However, detailed mineralogical inspection of carbonated cement samples (either experimentally or in real injection wells, SACROC) shows that metastable CaCO<sub>3</sub> polymorphs (aragonite and vaterite) can form and even be preserved, ruling out the local equilibrium assumption. The metastable nucleation and persistence of these carbonates can be understood in the frame of the Ostwald crystallization rule where nucleation kinetics of metastable forms is relatively high whereas transformation kinetics towards the most stable form (*i.e.*, calcite) is relatively slow. In the present study, for the first time, the 2-D distribution of CaCO<sub>3</sub> polymorphs in experimentally carbonated Portland cement cores is assessed using a new line-scanning setup for Raman mapping (Bernard et al., in press) combined to powder X-ray micro-diffraction performed on selected areas. The measured carbonate distribution is interpreted on basis the of a 1-D reaction-transport numerical model using kinetics data for CaCO<sub>3</sub> precipitation and dissolution from the literature. These data on calcium carbonate distribution will contribute to the effort of simulating Portland cement carbonation under relevant borehole boundary conditions for realistic cement chemistry.

## **2. Materials and methods**

### **2.1 Carbonation procedure**

Portland cement cores (Class G oilfield cement, slurry density=1.89 g/cm<sup>3</sup>, 30-mm diameter, 65-mm length) are prepared according to ISO/API Specifications 10, section 5 using fresh water. They are cored from a cement slurry cured in cubic molds for 72 hours at 21 MPa and 90°C, and stored in water. Then, they are loaded without removing the porous water in a high-pressure and high-temperature vessel for CO<sub>2</sub> exposures. The experimental set-up used in the present study has been extensively described elsewhere (Barlet-Gouédard et al., 2006; 2007; Rimmelé et al., 2008) and will be only outlined here. Water is first loaded into the vessel and pressure is increased by pumping CO<sub>2</sub> under the liquid state. The vessel is then externally heated up to 90°C and high pressure, 30 MPa, is reached. Two gravity separated fluids occur in the vessel: CO<sub>2</sub>-saturated water at the bottom of the reactor

and water-saturated CO<sub>2</sub>, i.e. wet supercritical CO<sub>2</sub>, at the upper half of it. Samples are piled up in the vessel in such a way that part of them is in contact with CO<sub>2</sub>-saturated water whereas others are only exposed to wet supercritical CO<sub>2</sub>. At the end of the experiments, temperature is first decreased and then pressure is slowly (a few hours) released by opening the pressure release valve manually. A longitudinal and/or horizontal section of the sample is then cut for further phase characterization.

## 2.2 Characterization techniques

Characterization of the mineralogical changes encountered in the Portland cement cores after being exposed to a CO<sub>2</sub>-rich fluid is performed by combining Raman micro-spectroscopy, X-ray diffraction and scanning electron microscope (Hitachi, S-2500) equipped with an Energy Dispersive Spectrometer (Thermo-Noran).

X-ray micro-diffraction patterns are obtained from less than 0.05 mm<sup>3</sup> of sample powder, picked up with a 0.5-mm diameter drill. The first 100 micrometers of the samples surface are removed to avoid superficial carbonates formed by secondary carbonation in air. The powder is then glued on a polymer fiber which is centered and spins at the focal of a high flux X-ray beam (parabolic mirror system from OSMIC, Inc) collimated at 300 µm. Current conditions for generating the X-ray beam were set to 200 mA and 40 kV as generated by a rotating copper anode (Rigaku – 18 kW max.). The diffracted-beam intensity is collected with an INEL CPS-120 detector (at ENS, Paris) with accumulation times of around 20 minutes.

Raman data are collected using a Renishaw® InVia Raman microspectrometer (at ENS, Paris) equipped with a 785 nm near infrared diode laser, a 1200 grooves/mm holographic grating and a RENCAM 2d CCD detector. For point analysis, performed at room temperature, the laser was focussed through a Leica DMLM microscope with a x50 objective (numerical aperture NA = 0.75). The signal was analyzed with a RENCAM CCD detector (400\*576 pixels). This configuration yields a planar resolution of around 2 or 3 µm and adjusting the laser power, which is initially of 300 mW, avoids laser-induced heating/damaging of the sample. Point by point Raman mapping with a sampling step of about 1 µm (only limited by the minimum laser spot size which is 1 µm) and a spectral

resolution of  $2.26\text{ cm}^{-1}$  has been achieved. Using an XYZ motorized stage supplied by Prior Scientific with a mechanical precision of  $0.1\text{ }\mu\text{m}$  in (x,y) allows to control the spatial resolution. To map large areas up to a few  $\text{mm}^2$  without drastically increasing the total acquisition time, we used the StreamLine mapping tool recently developed by Renishaw and described by Bernard et al. (in press). In this system, the exciting laser beam is used to illuminate a line on the sample along which multiple Raman spectra are recorded simultaneously. This exciting line on the sample is produced using a cylindrical lens before the microscope which can be moved in and out of the optical path to provide point or line illumination. Using a 50x objective the laser line is about  $25\text{-}\mu\text{m}$  long (Y) and  $1\text{-}\mu\text{m}$  wide (X), both displaying Gaussian distributions of intensity to a first approximation. This configuration shortens drastically the total acquisition time by up to 50 times compared to point mapping and makes possible the mapping of large areas with high imaging resolution, with a sampling step down to  $1.1\text{ }\mu\text{m}$ , only limited by the minimum spot size which is  $1 \times 1.1\text{ }\mu\text{m}$  (Bernard *et al.*, in press). In this line focus configuration, the laser power is also well below the threshold resulting in radiation damage to the sample. In addition, each data point is *in fine* illuminated by the whole line thanks to the total synchronization of the Raman signal acquisition on the CCD detector with the mechanical displacement of the XY motorized stage. Signal to noise ratios are then homogeneous over the map whatever the exciting line intensity profile (Bernard *et al.*, in press; Chopin *et al.*, in press). Each measured spectrum is subsequently compared to reference spectra (peak position, width and intensity) using a principal component analysis method provided by the Renishaw software (Wire 3.0). A correlation index is calculated for each point. Index values are comprised between 0 and 1, with 1 indicating full correlation with the reference spectrum, thus allowing semi-quantitative information to be determined for the whole area. In the maps presented here, a specific color is assigned to each particular reference mineral spectrum. Each pixel of the mapped area displaying an index value greater than 0.7 for a particular reference (in order to take into account the signal noise) has been represented in the specific colour of this reference.

### 2.3 Numerical modelling

The reactive transport of CO<sub>2</sub> through the pore water of Portland cement can be summarized as follows (Figure 1A): the pH contrast between the Ca-free CO<sub>2</sub>-saturated water (pH = 2.9 at 90°C, 30 MPa and the simplified-cement (i.e., with portlandite as single carbonating phase) pore water pH 10.2 at 90°C) drives H<sup>+</sup> (inward) and Ca<sup>2+</sup> (outward) diffusion. This diffusion process leads to portlandite under-saturation and to the dissolution of this mineral. At the same time, the inward diffusion of CO<sub>2</sub> aqueous species brings Ca-carbonate to saturation. Ultimately, these calcium carbonates may dissolve if the boundary conditions (CO<sub>2</sub> saturation, constant pH and Ca-free solution) are maintained. We modelled this whole process using a simple 1D reaction-diffusion code based on finite volumes. The main CO<sub>2</sub> diffusion direction (1D) is decomposed into a series of cells (mesh) containing a mineral assemblage composed of portlandite spread in an inert porous matrix. The presence of C-S-H phases is ignored in this simple model in order to avoid the complexity of dealing with a solid solution series of poorly known behaviour in CO<sub>2</sub>-rich environments (Corvisier et al., 2008). The computer code calculates the space and time variations of both volume fraction of solid-phases and composition of aqueous pore-solution composition. Obviously, pressure and temperature are assumed to be homogeneously distributed and constant throughout the sample. The model consists in the following set of equations [1] including N<sub>elt</sub> chemical element conservation laws, N<sub>aq</sub> mass action laws for aqueous species equilibria and N<sub>min</sub> kinetic laws for water/mineral interactions, for each mesh:

$$\left\{ \begin{array}{l} \frac{\partial}{\partial t} \left( \sum_{i=1}^{N_{aq}} \alpha_{l,i} n_i^{aq} \right) - \frac{\partial}{\partial x^2} \left( \sum_{i=1}^{N_{aq}} \alpha_{l,i} D_i^{eff} n_i^{aq} \right) + \left( \sum_{m=1}^{N_{min}} \beta_{l,m} \vartheta_m \right) = 0, \forall l \in [1, N_{elt}] \\ \left( \sum_{k=1}^{N_{elt}} \nu_{j,k} \log a_k \right) - \log a_j - \log K_j = 0, \forall j \in [N_{elt} + 1, N_{aq}] \\ \frac{\partial \phi_m}{\partial t} - \frac{V_m}{V_{tot}} \vartheta_m = 0, \forall m \in [1, N_{min}] \end{array} \right. \quad [1]$$

where  $\nu_{i,H_2O}$  denotes the number of H<sub>2</sub>O molecules in the aqueous species  $i$ ,  $\mu_{H_2O,m}$  is the number of H<sub>2</sub>O molecules in the mineral  $m$ ,  $z_i$  is the charge of the aqueous species  $i$ ,  $\alpha_{l,i}$  is the number of element  $l$  in the aqueous species  $i$ ,  $n_i^{aq}$  is the number of moles of the aqueous species  $i$  in the current mesh.  $D_i^{eff}$  is the effective diffusion coefficient for the aqueous

species  $i$  (Garboczi & Bentz, 1992),  $\beta_{l,m}$  the number of element  $l$  in mineral  $m$ ,  $v_m$  the precipitation/dissolution rate for mineral  $m$ ,  $v_{j,k}$  the stoichiometric coefficient of aqueous species  $k$  in the forming reaction of the aqueous species  $j$ ,  $a_k$  the activity (determined by an extended Debye-Hückel model) for the aqueous species  $k$ ,  $K_j$  the equilibrium constant for the formation reaction of the aqueous species  $j$ ,  $\phi_m$  the volume fraction of mineral  $m$ ,  $V_m$  the molar volume for the mineral  $m$  and  $V_{tot}$  the current mesh volume.

Water/minerals kinetic laws are based on the Transition State Theory (TST, Lasaga [1981, 1998]) and can be written as follows:

$$v_m = \begin{cases} k_m^p s_m \left( \frac{Q_m}{K_m} - 1 \right)^{\delta_m^p} \\ - k_m^d s_m \left( 1 - \frac{Q_m}{K_m} \right)^{\delta_m^d} \end{cases} \quad [2]$$

where  $k_m$  denotes the kinetic constant for precipitation/dissolution of mineral  $m$ ,  $K_m$  the equilibrium constant,  $Q_m$  the ionic activity product of the solution ( $Q_m/K_m - 1$  or  $1 - Q_m/K_m$  is the saturation degree measuring the gap to equilibrium) and  $\delta_m$  a mineral-specific empirical coefficient.

$s_m$  is the reactive surface calculated considering a solid-sphere model (a packing of ideal, disjointed spherical grains):

$$s_m = c_m s_m^0 \left( \frac{r_m}{r_m^0} \right)^2 \quad [3]$$

where  $c_m$  denotes a reactive coefficient which adjust the geometric surface to the reactive surface for the mineral  $m$  (Brosse et al., 2005),  $s_m^0$  the initial reactive surface,  $r_m^0$  the initial grain radius and  $r_m$  the current grain radius.



### 3. Phase characterization results

#### 3.1 Main carbonation features

The mineralogical and porosity changes encountered in Portland cement samples when exposed to CO<sub>2</sub>-rich fluids have been fully described in previous experimental studies (Barlet-Gouédard *et al.*, 2007; Rimmelé *et al.*, 2008) performed using the same experimental procedure (90°C, 28 MPa) on rigorously identical cement samples. These studies show that the pH contrast between acidic CO<sub>2</sub>-fluids and cement, as mentioned above, leads to relatively fast reactions (at least compared to species diffusive transport) which involve both carbonation and dissolution of the cement medium. Thus, the alteration process is characterized by a complex series of reactive fronts (Barlet-Gouédard *et al.*, 2007; Rimmelé *et al.*, 2008; Figure 1B). Practically, these reactions are materialized by significant porosity changes (Rimmelé *et al.*, 2008) as well as the formation of an alteration front (Figure 2A), the propagation of which is controlled by aqueous species diffusion through the porosity of the cement medium (Corvisier *et al.*, 2008). Large aragonite crystals (mm in size) appear to nucleate and grow onto the cement cores surface (Figure 2A). Fresh cement, *i.e.* before carbonation, is mainly composed of portlandite, Ca(OH)<sub>2</sub> or CH, and calcium silicate hydrates (C-S-H) which form most of the cement matrix. Remaining unhydrated grains of dicalcium silicate (Ca<sub>2</sub>SiO<sub>4</sub> or C<sub>2</sub>S) and of tricalcium silicate (Ca<sub>3</sub>SiO<sub>5</sub> or C<sub>3</sub>S), and tetracalcium aluminoferrite, (CaO)<sub>4</sub>.Al<sub>2</sub>O<sub>3</sub>.Fe<sub>2</sub>O<sub>3</sub> or C<sub>4</sub>AF, can also be observed (Figure 2B). Whatever the CO<sub>2</sub>-rich fluid (CO<sub>2</sub>-saturated water or wet supercritical CO<sub>2</sub>), in the carbonated zone of cements, apart from C<sub>4</sub>AF, all the Ca-bearing phases initially present have reacted to form calcium carbonates (mainly calcite and aragonite + traces of vaterite) along with amorphous silica gel (Figure 2C). Reminiscent C-S-H with very low Ca/Si ratio (0.2 - 0.3) are possibly preserved but portlandite has fully reacted. The occurrence of the three calcium carbonate polymorphs is an evidence of disequilibrium in the carbonated zone of the sample and tends to indicate that the role of kinetic factors cannot be ignored for calcium carbonate precipitation. In turn, the distribution of metastable CaCO<sub>3</sub> polymorphs can give information on the physical and chemical conditions having prevailed locally within the carbonated samples.

### 3.2 CaCO<sub>3</sub> polymorph distribution along the main diffusion path

The CaCO<sub>3</sub> polymorph distribution-profile across the sample can be determined using micro-focused XRD on powder collected from a cross-section of core sample ENS90-35T (Figure 3; Table 1). The use of around 0.05 mm<sup>3</sup> of sample only is responsible for the relatively poor signal/noise ratio of the corresponding diffraction patterns. However, the three CaCO<sub>3</sub> polymorphs can easily be identified with this technique (Figure 3). For example, the absence of carbonates in the cement sound zone (inner part of the sample) along the profile can be confirmed whereas the three polymorphs: calcite, aragonite and vaterite are observed in the carbonated zone. Vaterite is mainly concentrated in the vicinity of the sound zone, in the very thin “carbonation front”, ahead of the carbonated zone (Table 2).

Raman micro-spectrometry can also be used to identify the different CaCO<sub>3</sub> polymorphs and it offers a much better spatial resolution (down to 1 μm) than XRD. Raman spectroscopy has already been successfully applied to the characterization of cement phases and their hydration/carbonation (Tarrida et al., 1995; Kirkpatrick et al., 1997; Deng et al., 2002; Martinez-Ramirez et al., 2003; Potgieter-Vermaak et al., 2006; Martinez-Ramirez et al., 2006; Ibáñez et al., 2007). On the un-carbonated part of the samples (N100-523T), the use of an incident near infra-red laser (785 nm) reduced fluorescence effects and allowed the identification of the major cement phases: portlandite, C<sub>2</sub>S, C<sub>3</sub>S, C<sub>4</sub>AF and also gypsum, CaSO<sub>4</sub>·(H<sub>2</sub>O)<sub>2</sub> (Figure 4). However, the abundant C-S-H, which composes the cement matrix, yielded a very noisy Raman signal dominated by fluorescence. Nevertheless, calcite, aragonite and vaterite have been unambiguously distinguished within the carbonated edges of the samples. These three CaCO<sub>3</sub> polymorphs can coexist within sample areas of less than 40 × 40 μm<sup>2</sup> (Figure 5). The different Raman active vibration modes of calcium carbonates between 100 and 1200 cm<sup>-1</sup> are summarized in Table 3. The ν<sub>1</sub> (symmetric stretch) CO<sub>3</sub> vibration mode is characterized by a very strong band located at 1086 cm<sup>-1</sup> for calcite, aragonite and vaterite. Nevertheless, in addition to this CO<sub>3</sub> vibration mode, vaterite Raman spectrum also exhibits two intense Raman bands at 1092 cm<sup>-1</sup> and 1077 cm<sup>-1</sup>. This band triplet is specific to the vaterite spectrum and can thus be used to unambiguously identify this CaCO<sub>3</sub> polymorph. In the lattice vibration frequency range, calcite spectrum displays two weak bands at 279 and 154 cm<sup>-1</sup>, while four different Raman bands, centred at 279,

205, 152 and 143  $\text{cm}^{-1}$ , can be observed in aragonite spectrum and five weak bands, located at 302, 277, 205, 152 and 112  $\text{cm}^{-1}$ , are indicative of the vaterite spectrum. As an example of Raman mapping in a point-by-point configuration (680-1220  $\text{cm}^{-1}$  spectral range), the spatial distribution of vaterite has been studied around a residual (anhydrous)  $\text{C}_2\text{S}$  grain within the carbonated rim of N100-523T (1681 Raman spectra have been collected over a  $80 \times 80 \mu\text{m}^2$  area at a sampling step of 2.0  $\mu\text{m}$  in both x and y directions). As shown in Figure 6, vaterite has crystallized in close vicinity of the  $\text{C}_2\text{S}$  grain whereas aragonite and calcite compose the rest of the carbonated matrix (aragonite and calcite cannot be unambiguously distinguished in that spectral range). Moreover, a large vaterite area ( $40 \times 20 \mu\text{m}^2$ ) has been identified in the ‘shadow-region’ of the grain regarding the  $\text{CO}_2$  diffusive flow direction.

In order to map the whole carbonated zone from rim to core without drastically increasing the total acquisition time, dynamic line-scanning Raman mapping experiments have been performed. The same region of the sample ENS90-051B has been mapped twice (Figure 7), over two distinct spectral ranges: from 900 to 1300  $\text{cm}^{-1}$  to assess the spatial distribution of vaterite, and from 125 to 525  $\text{cm}^{-1}$  to distinguish aragonite and calcite (144153 Raman spectra have been collected over a  $1009 \times 4974 \mu\text{m}^2$  area at a sampling step of 5.9  $\mu\text{m}$  in both x and y directions). At this scale, the high concentration of vaterite on a 500  $\mu\text{m}$  wide zone at the carbonation front is clearly visible. The rest of the carbonated matrix is mostly composed of calcite and aragonite, the latter apparently being the dominant polymorph.

#### 4. Numerical simulations and Discussion

The formation of unexpected metastable  $\text{CaCO}_3$  polymorphs such as aragonite and vaterite in addition to calcite during cement carbonation processes has already been reported (Deng et al., 2002; Martinez-Ramirez et al., 2003; Potgieter-Vermaak et al., 2006; Martinez-Ramirez et al., 2006). In cement samples recovered from a  $\text{CO}_2$  injection well in the SACROC formation (Texas), the same  $\text{CaCO}_3$  polymorphs have been identified (Carey et al., 2007). Similar disequilibria, within sedimentary rocks containing calcite, aragonite,

Mg-rich calcites and also proto-dolomite have been reported (Morse & Casey, 1988). Moreover, using a purely reactive model, Morse & Casey (1988) demonstrated that the apparition of intermediate phases in the formation of a final product is controlled by kinetics. We show here, for the first time, that vaterite is mainly concentrated in a 500  $\mu\text{m}$  wide zone located ahead of the carbonated zone, the so-called carbonation front. In order to examine the thermochemical significance of this zone with respect to the cement carbonation process, we have developed a simple numerical model which accounts for the competition between the dissolution and the precipitation of the various  $\text{CaCO}_3$  polymorphs. Precipitation kinetic parameters for calcite and vaterite have been measured by Brečević & Kralj (2007). Since there is no consistent kinetic database for all three  $\text{CaCO}_3$  polymorphs, aragonite and calcite will not be distinguished in the following. This assumption is supported by a similar distribution of these two phases in the carbonated zone. In addition, the lack of dissolution kinetic values, led us in a first approach, to assume that precipitation and dissolution kinetic constant for calcite and vaterite are identical. This assumption is generally verified close to equilibrium. The aqueous solubility of calcite and vaterite are taken from Plummer et al. (1982). The thermochemical and kinetics data considered here are summarized in Table 4. Assuming the precipitation/dissolution kinetic law [2] and constant reactive surface areas (this latter assumption can be considered as reasonable at the beginning of  $\text{CaCO}_3$  precipitation where the contribution of surface areas is negligible compared to the kinetic effect of a high saturation degree), the competition between these two  $\text{CaCO}_3$  polymorphs can be visualized by plotting their respective kinetics versus the ionic activity product which indicates if the mineral will tend to precipitate or dissolve regarding the solution composition (Figure 8). In the course of carbonation experiments, when portlandite starts dissolving, the cement pore-water gets quickly oversaturated regarding calcium carbonates. The system is then in Zone 1 of Figure 8, where vaterite forms at a faster rate than calcite. However, subsequent calcium consumption decreases the saturation level and brings the system into Zone 2 (Figure 8). There, both calcite and vaterite precipitate, calcite precipitation kinetics is a little faster. Solution saturation with respect to  $\text{CaCO}_3$  keeps decreasing and the system enters Zone 3 (Figure 8). Then, calcite keeps precipitating while vaterite starts dissolving with a relatively fast rate. Finally at the end of the longer experiments, Zone 4 is reached and calcite starts dissolving slowly.

Keeping in mind this important competition between the processes of calcite and vaterite precipitation/dissolution, the evolution of a simplified cement material can be simulated numerically. We recall that this simplified cement (20% porosity) is composed of portlandite (20% of volume fraction),  $\text{Ca}(\text{OH})_2$  and a non-reactive phase (60 vol.%), and is submitted to a diffusive flux of  $\text{CO}_2$ -saturated water at  $90^\circ\text{C}$  and 30 MPa (all species are assumed to have the same aqueous diffusion coefficient of  $6.7 \cdot 10^{-9} \text{ m}^2 \cdot \text{s}^{-1}$ ). Possible pressure gradients within the sample are neglected here. The total calcium carbonate volume fraction versus sample depth is plotted in Figure 9 for simulation durations comprised between 6 and 84 hours. Both the carbonation front and the dissolution back-front described by Barlet-Gouédard et al. (2007) are present (Figure 9). As expected for a diffusive process, the propagation rate of these fronts follows a square-root of time law. We can also notice that the  $\text{CaCO}_3$  volume fraction equals to up to 23 vol. % of the sample, *i.e.* more than the initial portlandite volume proportion of 20%. Although vaterite forms prior to calcite in the course of the carbonation process, it is more rapidly dissolved and vaterite is then partly replaced by calcite (Figure 10). Consequently, after 12 hours, vaterite is more abundant than calcite at the front of the carbonate-rich zone whereas its abundance decreases towards the sample rim where calcite becomes the dominant carbonate. Therefore the calcite-rich zone seems to grow at the expense of the vaterite-rich one.

We define here the so-called “carbonation front” (see Rimmelé et al., 2008) as the carbonate-rich zone where the vaterite volume fraction is higher to ca. 5 %. The zone corresponds to a minimum of porosity. After 84 hours of simulation, this “carbonation front” is 0.35 mm wide whereas the calcite-dominant zone is 0.40 mm wide (Figure 10), *i.e.*, a carbonate rim of 0.75 mm has developed.

A carbonate distribution consistent with the experimental data is achieved when using an initial geometric surface of  $0.72 \text{ m}^2 \cdot \text{m}^{-3}$  for both calcite and vaterite seeds. Then, the observed carbonate grain size (ca.  $10 \mu\text{m}$ , Figure 2C) is satisfactorily simulated by setting the reactive coefficient to around 0.02. This coefficient can be understood as the portion of the carbonate grain surface available for growth but then it is expected to vary over time. Its low value may be related to the low porosity of the carbonated zone.

Due to the boundary conditions of an infinite acidic water reservoir saturated with  $\text{CO}_2$ , vaterite formed in a first stage will start dissolving, and therefore calcite formation will be enhanced. In a later stage, vaterite is completely replaced by calcite which is also expected to dissolve at some stage as a consequence of fixed boundary conditions. The numerical simulation presented here reproduces, at least qualitatively, the  $\text{CaCO}_3$  distribution in our samples inferred using Raman spectroscopy, i.e., a vaterite-rich zone ahead of the carbonation front with the more stable calcium carbonates located behind. However, the simulated width of the vaterite rim which mostly depends on both vaterite dissolution and calcite (and aragonite) precipitation rates, is different to the observed one. Using our code, we can try to constrain the vaterite dissolution constant which was taken, in a first step, as equal to its precipitation one as measured by Brečević and Kralj (2007). Several simulations with various vaterite dissolution coefficients comprised between 3.23 and  $0.03 \text{ mol.m}^{-2}.\text{h}^{-1}$  were run to adjust this parameter to the observed vaterite front thickness (Figure 11). This yielded a vaterite dissolution coefficient equals to  $1.6 \text{ mol.m}^{-2}.\text{h}^{-1}$  which is about twice as low as its precipitation constant and about a hundred time higher than the calcite precipitation one. It must be recalled here that it is the competition between calcite precipitation and vaterite dissolution rates which mostly controls the vaterite front thickness.

## 5. Concluding remarks

The preservation of a metastable  $\text{CaCO}_3$  polymorph such as vaterite in Portland cement carbonated according to a reactive-transport process has the following consequences:

- Local equilibrium in reaction-transport code applied to Portland cement carbonation cannot be assumed as long as calcium carbonates are concerned.
- The occurrence and the size of a vaterite-rich zone in carbonated Portland cements is a proxy of local over-saturation which relates to the boundary conditions (e.g.,  $\text{CO}_2$  rich fluid composition). Under controlled experimental conditions, dissolution and precipitation kinetic parameters can be constrained.

- The volume variation associated with the carbonation of solid cement matrix (*e.g.*, portlandite and C-S-H) will depend on the CaCO<sub>3</sub> form which precipitates. The volume difference of 2 – 2.5 % between vaterite and calcite is far from being negligible. Recently, Rimmelé et al. (2008) have shown using SEM imaging in backscattered electron mode that the 2D relative porosity obtained by BSE image analysis of the carbonated sample portion is low and can reach less than 5 % in the zone that we inferred here to be vaterite rich. Potentially, the polymorphic transformation of vaterite into calcite would then lower that porosity by a factor 2.

- We confirm here that the combination of experimental and simple (1-D) modelling tools, offers a powerful approach to characterize and simulate the reactive transport of CO<sub>2</sub>-rich fluids in Portland cement. However, proper characterization of reacted cement porosity and mineralogy using characterization techniques such as micro-Raman mapping, X-ray micro-diffraction and chemical mapping (SEM) is required in order to interpret the experimental data and constrain the numerical model. In this respect, the understanding of the carbonation behaviour of C-S-H phases which are difficult to characterize using conventional techniques remains a major challenge for a realistic simulation of Portland cement carbonation.

## 6. References

- Barlet-Gouédard, V., Rimmelé, G., Goffé, B. & Porcherie, O. (2006): Mitigation strategies for the risk of CO<sub>2</sub> migration through wellbores. *SPE 98924, International Association of Drilling Conference, Miami, Florida - USA*.
- Barlet-Gouédard, V., Rimmelé, G., Goffé, B. & Porcherie, O. (2007): Well technologies for CO<sub>2</sub> geological storage: CO<sub>2</sub>-resistant cement. *Oil and Gas Science and Technology – Rev.IFP*, **62**, 325–334.
- Barlet-Gouédard, V., Rimmelé, G., Porcherie, O., Quisel, N. & Desroches, J.: A solution against well cement degradation under CO<sub>2</sub> geological storage environment. *International Journal Of Greenhouse Gas Control*, in press.
- Bernard, S., Beyssac, O. & Benzerara, K.: Raman mapping using advanced line-scanning systems: geological applications. *Applied Spectroscopy*, in press.

- Brečević, L. & Kralj, D. (2007): On calcium carbonates: from fundamental research to application. *Croatica Chemica Acta*, **80**, 467-484.
- Brosse, E., Magnier, C. & Vincent, B. (2005): Modelling fluid-rock interaction induced by the percolation of CO<sub>2</sub>-enriched solutions in core samples: the role of reactive surface area. *Oil and Gas Science and Technology – Rev.IFP*, **60**, 287–305.
- Bruckdorfer, R. (1986): Carbon dioxide corrosion in oilwell cements. *SPE 15176, Rocky Mountain Regional Meeting, Billings, Montana - USA*.
- Carey, J., Wigand, M., Chipera, S., WoldeGabriel, G., Pawar, R., Lichtner, P., Wehner, S., Raines, M. & Guthrie Jr., G. (2007): Analysis and performance of oil well cement with 30 years of CO<sub>2</sub> exposure from the SACROC Unit, West Texas, USA. *International Journal of Greenhouse Gas Control*, **1**, 75-85.
- Chopin, C., Beyssac, O., Bernard, S. & Malavieille, J.: Aragonite–garnet intergrowths in eclogite-facies marble, Alpine Corsica. *European Journal of Mineralogy*, in press.
- Corvisier, J., Fabbri, A., Brunet, F., Leroy, Y., Goffé, B., Rimmelé, G. & Barlet-Gouédard, V. (2008): A Numerical Model for CO<sub>2</sub> Wells Ageing through Water/Supercritical CO<sub>2</sub>/Cement Interactions. *3rd International Conference on Coupled T-H-M-C (thermal, hydraulic, mechanical, chemical) Processes in Geosystems, Lille - France*.
- Deng, C., Breen, C., Yarwood, J., Habesch, S., Phipps, J., Craster, B. & Maitland, G. (2002): Ageing of oilfield cement at high humidity: a combined FEG-ESEM and Raman microscopic investigation. *Journal of Materials Chemistry*, **12**, 3105-3112.
- Duguid, A., Radonjic, M. & Scherer, G. W. (2006): The effect of carbonated brine on the interface between well cement and geologic formations under diffusion-controlled conditions. *8th International Conference on Greenhouse Gas Control Technologies, Trondheim - Norway*.
- Fabbri, A., Corvisier, J., Schubnel, A., Brunet, F., Fortin, J., Goffé, B., Barlet-Gouédard, V., Rimmelé, G. & Leroy, Y. (2008): Effect of carbonation on the hydro-mechanical properties of Portland cements. *3rd International Conference on Coupled T-H-M-C (thermal, hydraulic, mechanical, chemical) Processes in Geosystems, Lille - France*.
- Garboczi, E. J. & Bentz, D. (1992): Computer simulation of the diffusivity of cement-based materials. *Journal of Materials Science*, **27**, 2083–2092.
- Huet, B., Fuller, R. & Prevost, J. (2006): Development of a coupled geochemical transport code to simulate cement degradation in CO<sub>2</sub> saturated brine. *8th International Conference on Greenhouse Gas Control Technologies, Trondheim - Norway*.
- Ibañez, J., Artus, L., Cusco, R., Lopez, A., Menendez, E. & Andrade, M. (2007): Hydration and carbonation of monoclinic C<sub>2</sub>S and C<sub>3</sub>S studied by Raman spectroscopy. *Journal of Raman Spectroscopy*, **38**, 61-67.
- Jacquemet, N., Pironon, J. & Saint-Marc, J. (2008): Mineralogical changes of a well cement in



- various H<sub>2</sub>S-CO<sub>2</sub>(-brine) fluids at high pressure and temperature. *Environmental Science and Technology*, **42**, 282-288.
- Kirkpatrick, R., Yarger, J., McMillan, P., Yu, P. & Cong, X. (1997): Raman Spectroscopy of C-S-H, Tobermorite and Jennite. *Advanced Cement Based Materials*, **5**, 93-99.
- Kontoyannis, C. & Vagenas, N. (2000): Calcium carbonate phase analysis using XRD and FT-Raman spectroscopy. *The Analyst*, **125**, 251-255.
- Kutchko, B., Strazisar, B., Dzombak, D., Lowry, G. & Thaulow, N. (2007): Degradation of well cement by CO<sub>2</sub> under geologic sequestration conditions. *Environmental Science and Technology*, **41**, 4787-4792.
- Lasaga, A. (1998): *Kinetic theory in the Earth sciences*, Princeton University Press.
- Lasaga, A. (1981): Transition state theory. *Reviews in Mineralogy – Kinetic of geochemical processes*, **8**, 135-169.
- Lietzke, M. & Stoughton, R. (1961): The calculation of activity coefficients from osmotic coefficients data. *Journal of Physical Chemistry*, **65**, 508–509.
- Martinez-Ramirez, S., Friaz, M. & Domingo, C. (2006): Micro-Raman spectroscopy in white portland cement hydration: long-term study at room temperature. *Journal of Raman Spectroscopy*, **37**, 555-561.
- Martinez-Ramirez, S., Sanchez-Cortes, S., Garcia-Ramos, J., Domingo, C., Fortes, C. & Blanco-Varela, M. (2003): Micro-Raman spectroscopy applied to depth profiles of carbonates formed in lime mortar. *Cement and Concrete Research*, **33**, 2063-2068.
- Moranville, M., Kamali, S. & Guillon, E. (2004): Physicochemical equilibria of cement-based materials in aggressive environments-experiment and modeling. *Cement and Concrete Research*, **34**, 1569–1578.
- Morse, J. & Casey, W. (1988): Ostwald processes and mineral paragenesis in sediments. *American Journal of Science*, **288**, 537-560.
- Nourtier-Mazauric, E., Guy, B., Fritz, B., Brosse, E., Garcia, D. & Clément, A. (2005): Modelling the dissolution/precipitation of ideal solid solutions. *Oil and Gas Science and Technology – Rev.IFP*, **60**, 401–415.
- Oelkers, E. & Helgeson, H. (1988): Calculation of the thermodynamic and transport properties of aqueous species at high pressures and temperatures: Aqueous tracer diffusion coefficients of ions to 1000°C and 5 kb. *Geochimica et Cosmochimica Acta*, **52**, 63-85.
- Ostwald, W. (1897): Studien über die bildung und umwaldung fester körper. *Zeitschrift für Physikalische Chemie*, **22**, 289-330.
- Plummer, L. & Busenberg, E. (1982): The solubilities of calcite, aragonite and vaterite in CO<sub>2</sub>-

H<sub>2</sub>O solutions between 0 and 90°C, and an evaluation of the aqueous model for the system CaCO<sub>3</sub>-CO<sub>2</sub>-H<sub>2</sub>O. *Geochemica et Cosmochemica Acta*, **46**, 1011-1040.

Potgieter-Vermaak, S., Potgieter, J. & Van Grieken, R. (2006): The application of Raman spectrometry to investigate and characterize cement, Part I: A review. *Cement and Concrete Research*, **36**, 656-662.

Potgieter-Vermaak, S., Potgieter, J., Belleil, M., De Weerd, F. & Van Grieken, R. (2006): The application of Raman spectrometry to the investigation of cement, Part II: A micro-Raman study of OPC, slag and fly ash. *Cement and Concrete Research*, **36**, 663-670.

Rimmelé, G., Barlet-Gouédard, V., Porcherie, O., Goffé, B. & Brunet, F. (2008): Heterogeneous porosity distribution in Portland cement exposed to CO<sub>2</sub>-rich fluids. *Cement and Concrete Research*, **38**, 1038-1048.

Tarrida, M., Madon, M., Le Rolland, B. & Colombet, P. (1995): An In-Situ Raman Spectroscopy Study of the Hydration of Tricalcium Silicate. *Advanced Cement Based Materials*, **2**, 15-20.

Yamada, Y., Tanaka, D. & Murata, S. (2006): Alteration of formation barrier due to CO<sub>2</sub> injection. *International Symposium on Site Characterization for CO<sub>2</sub> Geological Storage, Berkeley – USA*.

## Tables

sample	duration (days)	temperature (°C)	CO <sub>2</sub> pressure (MPa)	CO <sub>2</sub>
N100-523T	22	90	10	wet supercritical
ENS90-003B	3	90	30	dissolved in water
ENS90-035T	35	90	30	wet supercritical
ENS90-051B	51	90	30	dissolved in water

**Table 1** Summary of the sample carbonation conditions.

	front distance	aragonite	calcite	vaterite
I	0.7mm	yes	yes	no
II	-0.1mm	weak	weak	yes
III	0.1mm	yes	yes	yes
IV	0.5mm	yes	yes	no
V	-0.2mm	no	no	no
VI	0.4mm	yes	yes	weak
VII	-0.6mm	no	no	no

**Table 2** Sampling position regarding the carbonation front on the sample ENS90-035T and qualitative carbonate content based on the XRPD analysis.

calcite	aragonite	vaterite	vibration mode
		1092 vs	$\nu_1$
1086 vs	1086 vs	1086 vs	$\nu_1$
		1077 s	$\nu_1$
		751 vw	$\nu_4$
		738 vw	$\nu_4$
712 w		715 vw	$\nu_4$
	706 w	707 vw	$\nu_4$
	702 w		$\nu_4$
		302 w	lattice
278 w	278 w	277 w	lattice
	205 w	205 w	lattice
152 w	152 w	152 w	lattice
	143 w		lattice
		112 w	lattice

vs, very strong; s, strong; w, weak; vw, very weak.

**Table 3** Raman vibrations for the observed  $\text{CaCO}_3$  polymorphs.

	calcite	vaterite
$\log K^*$	-9.170	-8.697
$k^\# (\text{mol.m}^{-2}.\text{s}^{-1})$	$2.374 \cdot 10^{-5}$	$8.976 \cdot 10^{-4}$
$\delta^\#$	2	2
$s^0 (\text{m}^2.\text{m}^{-3})$	0.72	0.72
c	0.02	0.02
$\phi^0 (\%)$	$1.0 \cdot 10^{-8}$	$2.0 \cdot 10^{-8}$

\*Plummer & Busenberg (1982).

<sup>#</sup>Brečević & Kralj (2007).

**Table 4** Thermodynamic and kinetic data for calcite and vaterite at 90°C. Initial texture parameters (geometric surfaces, reactive coefficients and volume fractions) for numerical simulations.

## Figures

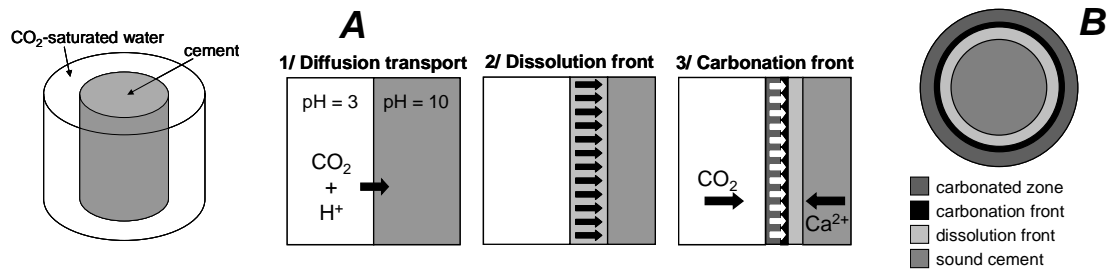


**Figure 1 (A)** Sketch showing the main mechanisms activated during the experimental carbonation. **(B)** Schematic view of a carbonated cement sample cross-section showing the different zones (and their terminology) induced by  $\text{CO}_2$  alteration.

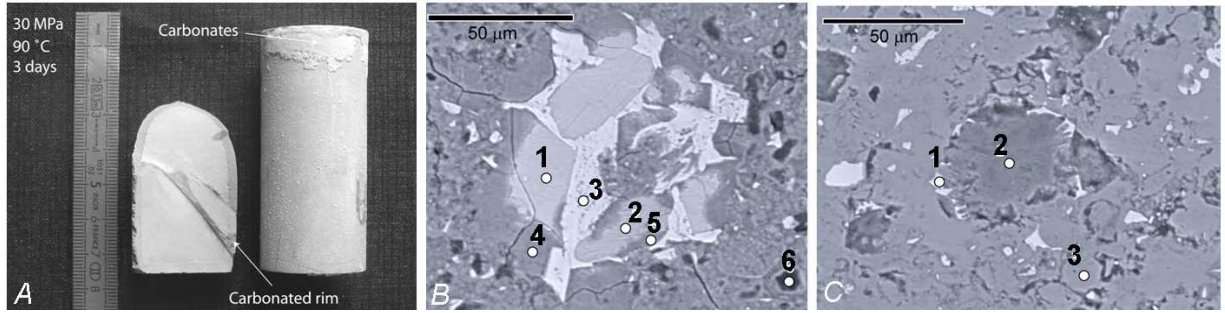


**Figure 2** (A) Example of a Portland cement sample ran for 3 days at 30 MPa, 90°C in CO<sub>2</sub>-saturated water (ENS90-003B). In addition to the carbonated rim (greyish zone visible on the cut sample), euhedral mm-size aragonite and calcite grains are found to crystallize onto the sample surface. (B) Hydration features in a fresh cement zone (sample N100-523T, BSE image). The empty circles locate the electron-microprobe spot: (1) C<sub>3</sub>S, (2) C<sub>2</sub>S, (3) C<sub>4</sub>AF, (4) C-S-H with Ca/Si = 2.1, (5) C-S-H with Ca/Si = 1.7, (6) portlandite. C-S-H rims can be distinguished around both C<sub>3</sub>S and C<sub>2</sub>S. (C) Carbonated rim of sample N100-523T (BSE). Refractory C<sub>4</sub>AF are preserved and show the same textures as in the fresh zones. (1) C<sub>4</sub>AF, (2) silica-gel rich zone, (3) rounded carbonate.



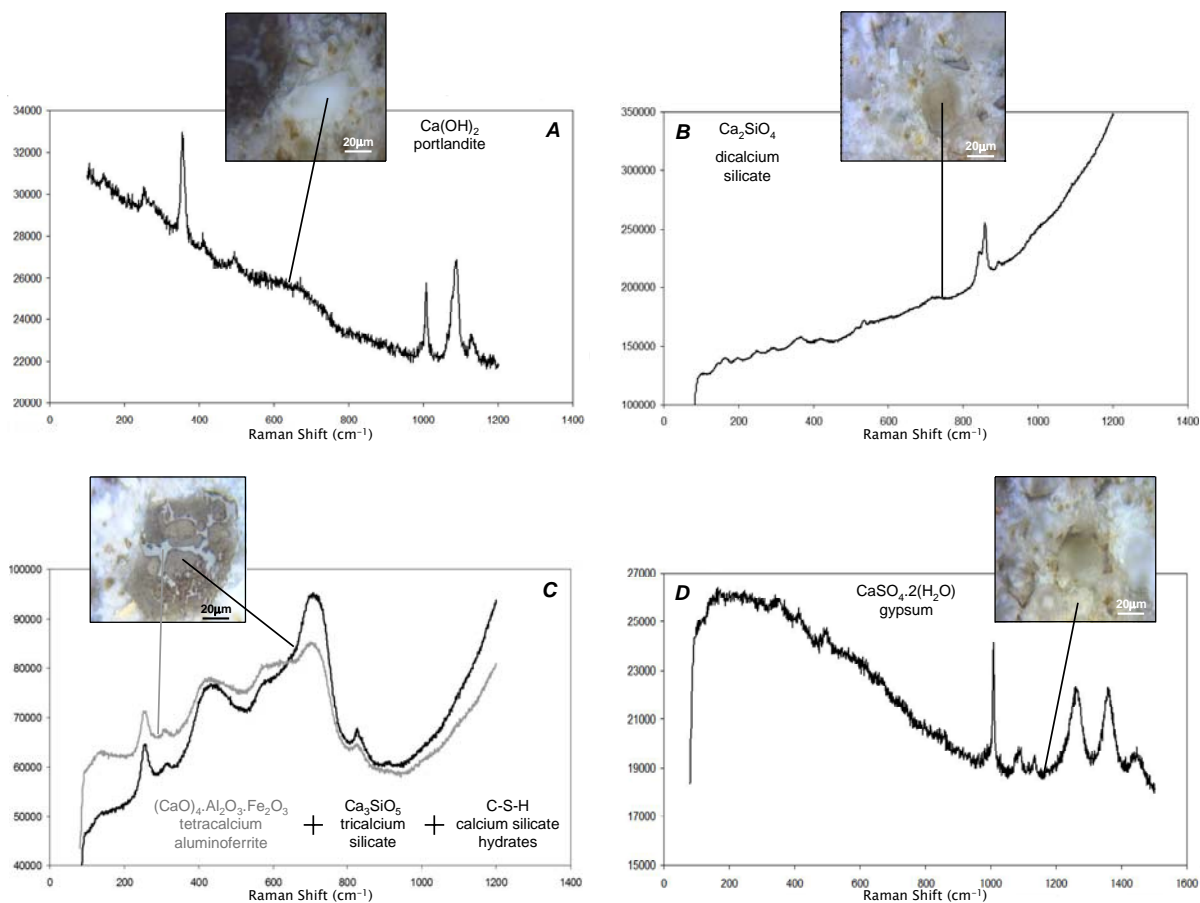


**Figure 4** Raman spectra of selected phases from sample N100-523T (Insets are optical images of the investigated areas in reflection mode). **(A)** portlandite, **(B)**  $C_2S$ , **(C)**  $C_3S + C_4AF + C-S-H$ , **(D)** gypsum.

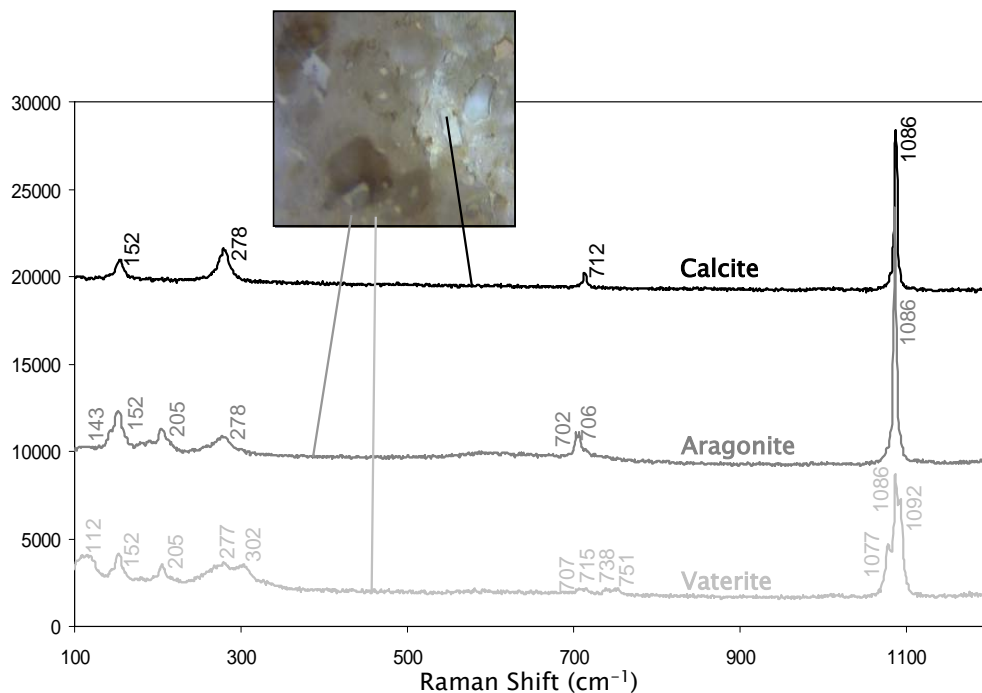


**Figure 5** Characteristic Raman spectra of the three  $\text{CaCO}_3$  polymorphs collected on sample N100-523T in the carbonated zone (Inset is an optical image of the investigated area in reflection mode).

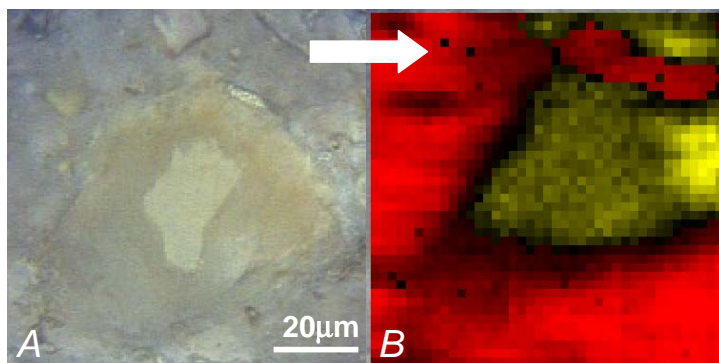


**Figure 6** (A) Optical image (reflected light) of a partially carbonated  $\text{C}_2\text{S}$  (N100-523T). (B) Corresponding component Raman map (compiled from 1681 Raman spectra collected over a  $80 \times 80 \mu\text{m}^2$  area, at a sampling step of  $2.0 \mu\text{m}$  in both x and y directions), showing the correlation index of each spectrum with the reference spectrum of vaterite (yellow) and calcite/aragonite (red). Higher index values (bright colours) indicate a greater correlation between measurement and reference. White arrow indicates the carbonation 'flow' direction. The vaterite is present around the  $\text{C}_2\text{S}$  grain, particularly in the 'shadow-region' regarding the flow. Calcite and aragonite abundantly occur everywhere else.

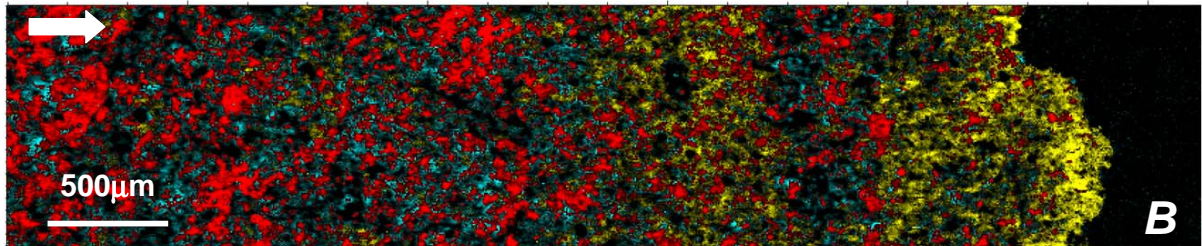
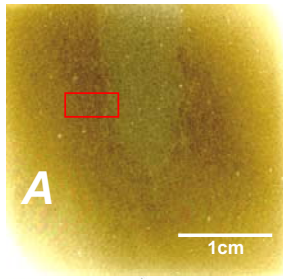


**Figure 7** Component dynamic line-scanning Raman map of the carbonated zone of ENS90-051B sample (mosaic compiled from 144153 Raman spectra collected over a  $1009 \times 4974 \mu\text{m}^2$  area, at a sampling step of  $5.9 \mu\text{m}$  in both x and y directions), showing the correlation index of each spectrum with the reference spectrum of vaterite (yellow), calcite (cyan) and aragonite (red). Higher index values (bright colours) indicate larger correlation index. White arrow indicates the carbonation 'flow' direction. At this scale, the high concentration of vaterite on a  $500 \mu\text{m}$  large zone at the carbonation front is clearly visible. A second vaterite-rich zone behind may well materialize a "paleofront" as defined by Barlet-Gouédard et al., 2006. The rest of the carbonated matrix is mostly composed of calcite and aragonite, the latter apparently being the dominant polymorph.

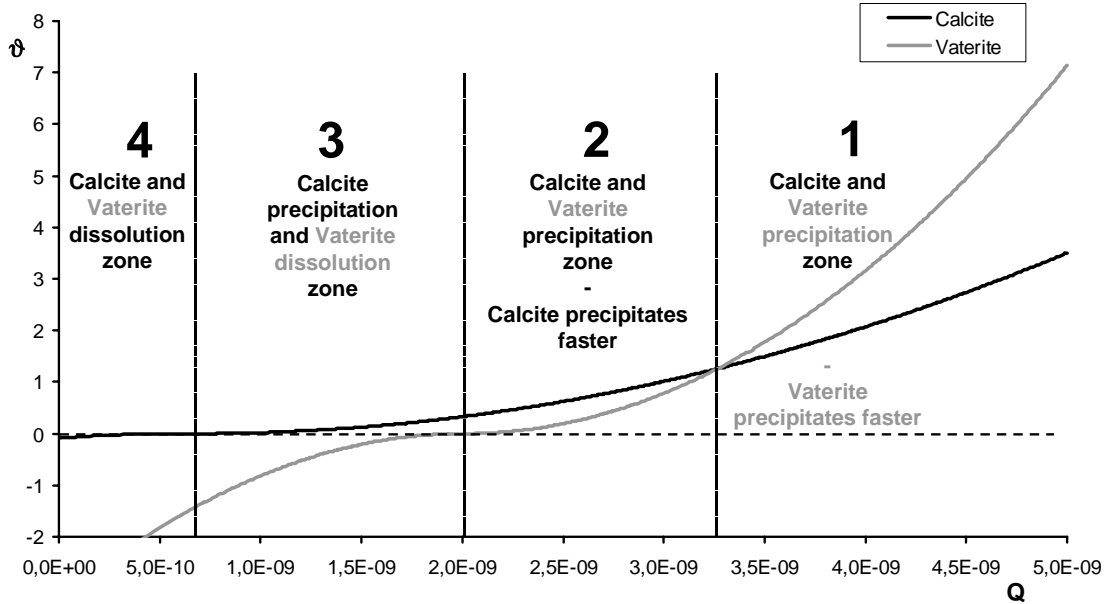


**Figure 8** Calcite and vaterite dissolution/precipitation kinetics ( $\vartheta$ ) versus aqueous solution ionic activity product. Portlandite dissolution and  $\text{CO}_2$  diffusion brings the solution to Zone 1.



Vaterite precipitates faster than calcite and, subsequently, lowers Q down to Zone 2 where calcite formation is the fastest. Once the fluid composition reaches Zone 3, there is a competition between vaterite dissolution (increase Q) and calcite crystallization (decrease Q). This competition controls the vaterite rim width.

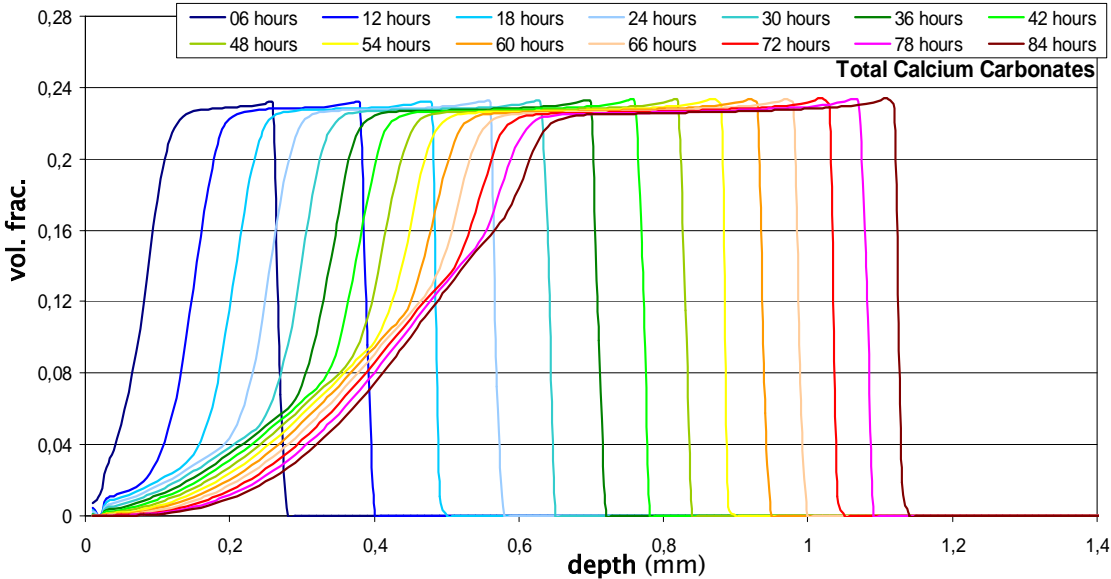


**Figure 9** Total calcium carbonates (calcite + vaterite) volume fraction as a function of depth (mm) for increasing run durations. The width of the carbonated front increases with time although it is partially dissolved by the acidic fluid (dissolution back-front).

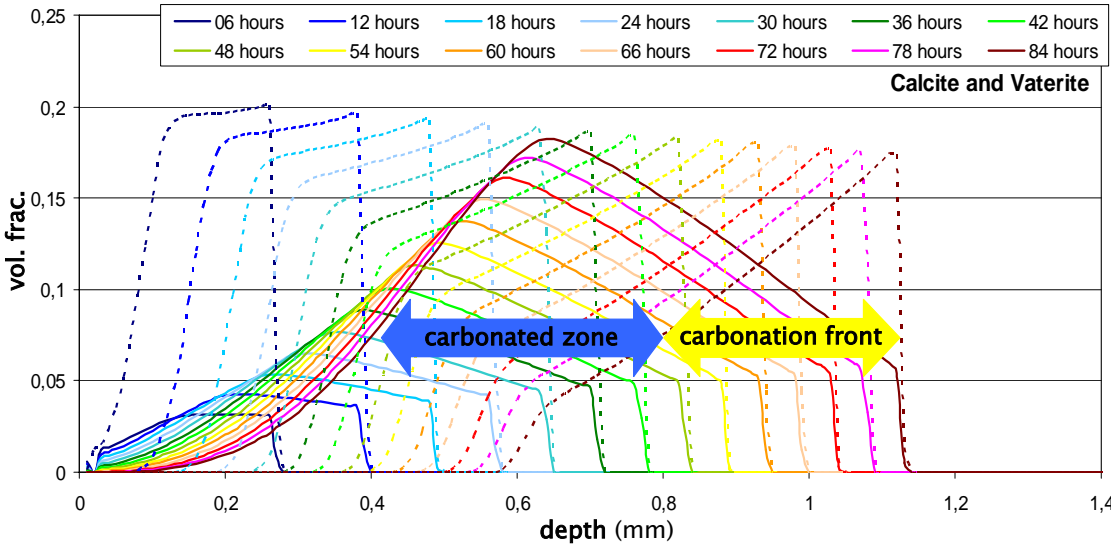


**Figure 10** Calcite (solid line) and vaterite (dash) volume fractions versus the depth (mm) for several run durations. The width of the vaterite rim remains roughly constant after 60-70 hours.

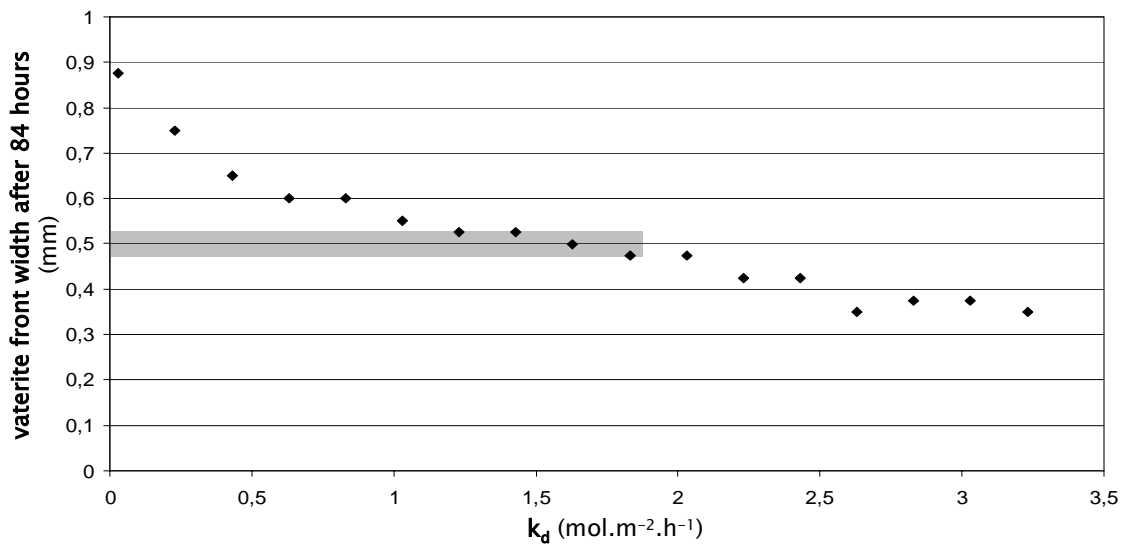


**Figure 11** Simulations with various dissolution kinetic constants for vaterite (from 0.03 to 3.23 mol.m<sup>-2</sup>.h<sup>-1</sup>) for a run duration of 84 hours. A vaterite-front width of 500 μm is achieved after 84 hours for a dissolution constant of around 1.6 mol.m<sup>-2</sup>.h<sup>-1</sup>.